

# Variational quantum eigensolver for the Heisenberg antiferromagnet on the kagome lattice

Joris Kattemölle<sup>1,2,\*</sup> and Jasper van Wezel<sup>1,2</sup>

<sup>1</sup>*Institute for Theoretical Physics, University of Amsterdam, Science Park 904, Amsterdam, The Netherlands*

<sup>2</sup>*QuSoft, CWI, Science Park 123, Amsterdam, The Netherlands*

Establishing the nature of the ground state of the Heisenberg antiferromagnet (HAFM) on the kagome lattice is well known to be a prohibitively difficult problem for classical computers. Here, we give a detailed proposal for a Variational Quantum Eigensolver (VQE) intending to solve this physical problem on a quantum computer. At the same time, this VQE constitutes an explicit experimental proposal for showing a useful quantum advantage on Noisy Intermediate-Scale Quantum (NISQ) devices because of its natural hardware compatibility. We classically emulate noiseless quantum computers with either 2D grid or all-to-all connectivity and simulate patches of the kagome HAFM of up to 20 sites. In all cases, the ground state energy, as found by the VQE, approaches the true ground state energy exponentially as a function of the circuit depth. Besides indicating the potential of quantum computers to solve for the ground state of the kagome HAFM, the classical emulation of VQEs serves as a benchmark for real quantum devices on the way towards a useful quantum advantage.

## I. INTRODUCTION

Despite decades of developments in numerical methods, the ground state properties of the Heisenberg antiferromagnet (HAFM) on the kagome lattice (Fig. 1) remain elusive, owing to its geometrical frustration. The kagome HAFM is the prime candidate for exhibiting a new phase of magnetism, the quantum spin liquid (QSL) [1–3], and forms a model for the magnetic properties of minerals like Herbertsmithite [4]. Approaches towards solving this ground state problem include exact diagonalization of finite-size patches [5] and the density matrix renormalization group (DMRG) method [2]. Next to the QSL, a Valence Bond Crystal (VBC) has been proposed as the ground state of the kagome HAFM [6–10]. (See Ref. [5] and references therein for a more complete overview of the techniques and proposals.) All classical methods for finding the ground state of the kagome HAFM are ultimately limited, for example by the inability to treat large patches (exact diagonalization), or the inability to describe highly entangled states (DMRG).

Quantum computation is a new player in this field that brings with it entirely novel possibilities. One method for finding ground states on a quantum computer is the Variational Quantum Eigensolver (VQE) [11, 12]. VQEs are especially suited for Noisy Intermediate-Scale Quantum (NISQ) [13] devices because of their relatively mild circuit depth requirements and inherent noise resilience [11, 12, 14, 15]. A VQE is a variational method. What sets the VQE apart from classical variational methods is that the parametrized state is obtained by applying a parametrized quantum circuit to some easy to prepare reference state of the quantum computer’s register. The energy of the resulting state is obtained by performing measurements on many copies of that state. (Generally,

the classical simulation of state preparation and measurement is intractable.) Parameter variation and optimization are still performed by a classical routine. So, a VQE can be seen as a classical variational method that uses a quantum computer as a subroutine for its function calls to the energy landscape.

Quantum computers can already outperform classical computers, and have hence obtained what is called ‘quantum supremacy’ or ‘a quantum advantage’ [16, 17]. However, the tasks for which quantum computers can currently outperform classical computers have no known application; these tasks were designed purely for showing a quantum advantage. The milestone of a *useful* quantum advantage, where a quantum computer performs a useful task that cannot be performed on any classical computer, is still ahead [16, 17].

In this work, we design a VQE for the kagome HAFM as an explicit proposal for showing a useful quantum ad-

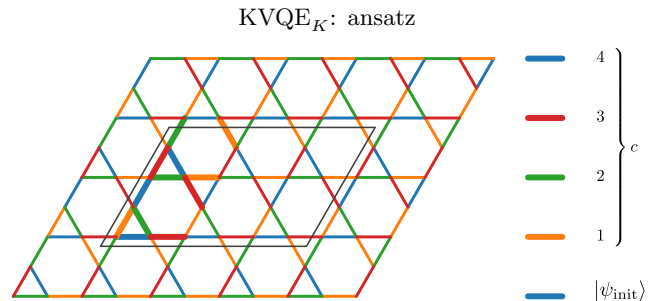


Figure 1. (Colour online.) The kagome lattice, with edges coloured according to a minimal edge colouring with the smallest possible colouring unit cell (thicker lines). The ansatz of KVQE<sub>K</sub>, with initial state  $|\psi_{\text{init}}\rangle$  and circuit cycle  $c$ , is derived from this edge-colouring by identifying every subset of edges having the same colour with a layer of parametrized gates. The grey parallelogram delineates a periodic patch that is simulated in this work.

\* Present address: University of Konstanz, Germany

vantage on NISQ devices and for a novel method for finding the ground state of the kagome HAFM. We explicitly consider the case where the quantum computer has the connectivity of a 2D grid. We refer to the resulting VQE as  $KVQE_G$  for short. We refer to the VQE as  $KVQE_K$  whenever we assume a quantum computer with at least kagome connectivity (this includes architectures with all-to-all connectivity). We tested  $KVQE_{G/K}$  by noiseless emulation on a classical computer in a host of cases, which are detailed in Sec. IID. For both  $KVQE_G$  and  $KVQE_K$ , the results of one case are reported in this paper. The remainder can be found in the Supplementary Material [18].  $KVQE_{G/K}$  only gives information about the ground state properties of finite size patches. As is standard practice in numerical methods, properties of the infinite system can be derived from a finite-size scaling approach, as in Ref. [19]. Such an approach is beyond the scope of the current work, since there are not enough patches for which it is tractable to emulate  $KVQE$  classically, but would be fully possible on a quantum computer with on the order of fifty qubits.

$KVQE_{G/K}$  uses the Hamiltonian Variational Ansatz (HVA) [20]. In the HVA, to find the ground state of a Hamiltonian  $H$ , the ansatz state is obtained by first preparing some known, easy-to-prepare ground state of a Hamiltonian  $H_{init}$ . Thereafter, this state is evolved sequentially by terms drawn from  $H$  and  $H_{init}$ . (Commuting terms may be evolved by simultaneously.) Every gate corresponds to time evolution along a term in  $H$  or  $H_{init}$ , where the parameter of that gate is set by the time duration of the evolution. The HVA itself does not specify  $H_{init}$  nor the sequence of terms the initial state is evolved by. Our choice of  $H_{init}$  and gate sequences for the cases presented in this work are detailed in Fig. 1 and Fig. 2.

In addition, we propose to run a similar VQE for the HAFM on the periodic chain as an intermediate goal. We call this VQE CVQE for short. It is similar to a VQE in Ref. [21]. Differences are that we simulate a periodic chain instead of an open chain, we use one parameter per gate instead of one parameter per layer, and that we go to larger system sizes and circuit depths. CVQE is a suitable benchmark problem for quantum hardware because, in contrast to the kagome lattice, the ground state of the HAFM on the chain can be computed efficiently classically through the Bethe ansatz [22–24]. This opens the possibility of comparing the optimal energy found by the VQE running on a quantum computer against the exact ground state energy, even for chains with hundreds of sites. It is only for systems up to approximately fifty qubits that similar benchmarks can be made for the kagome HAFM [5]. The explicit gate sequence we use for CVQE is depicted in Fig. 3.

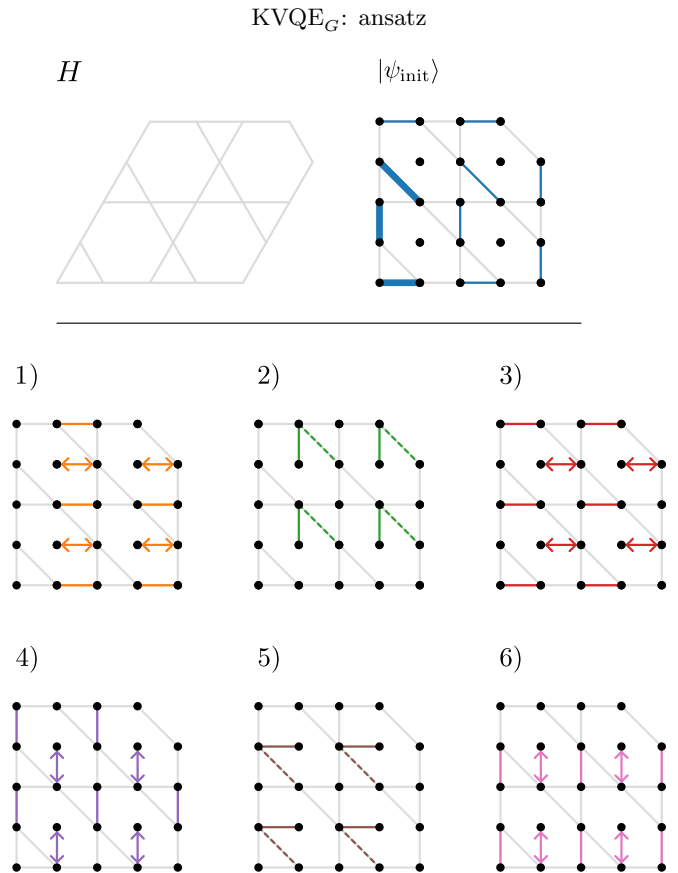


Figure 2. **(Top left)** The kagome lattice, of which only the 20-site open patch simulated by  $KVQE_G$  is shown. For the kagome HAFM, spin-1/2 particles are placed on the vertices, and the Heisenberg interaction is defined along the edges [Eq. (3)]. **(Top right)** The initial state  $|\psi_{init}\rangle$ . Black dots represent qubits and solid blue lines represent singlets. A sheered kagome lattice is added in the background in grey as a guide to the eye. The bolder solid lines form one unit cell of the dimer covering, which can be used to extend the current ansatz to systems of arbitrary size. For open boundaries, some patching of the regular dimer covering is needed. Here, this consists of the two singlets at the far right. **(Bottom)** The cycle  $c$  that is applied to  $|\psi_{init}\rangle$   $p$  times to obtain the ansatz state. Solid coloured lines represent  $HEIS(\alpha)$  gates. A  $HEIS(\alpha)$  gate evolves two qubits according to the Heisenberg exchange interaction for a time given by  $\alpha$  [Eq. (4)]. We use one parameter per  $HEIS$  gate, leading to  $M = 30p$  parameters in total. Two-headed arrows indicate SWAP gates. Dashed, coloured lines indicate along which bond of the kagome lattice the  $HEIS$  gates of that layer act effectively. The unit cell of the cycle equals that of the kagome lattice itself, and can hence be straightforwardly extended to larger system sizes.

### A. Hardware compatibility

For NISQ VQE algorithms to give an advantage over purely classical methods, the structure of the problem must be close to the quantum hardware the VQE is run on [25]. Especially  $KVQE_G$  is designed to be close to NISQ hardware. It is so for three reasons. Firstly, be-

cause the Hamiltonian of the kagome HAFM is a spin Hamiltonian, it is directly a Hamiltonian defined on qubits. In contrast, many Hamiltonians for which VQEs are proposed are fermionic. Examples include those in quantum chemistry [12, 14, 26], and the Fermi-Hubbard model [15, 20, 27, 28]. For a VQE to solve for the ground state of a Fermionic Hamiltonian, it first needs to be mapped to a spin Hamiltonian, for example by the Jordan-Wigner [29], Bravyi-Kitaev [30] or ternary tree [31] transformations. Fermion to spin maps either increase the non-locality of terms in the Hamiltonian or introduce additional qubits, in any case leading to overhead in quantum resources.

A second reason that KVQE<sub>G</sub> is close to NISQ hardware is that its gates are essentially native to multiple NISQ architectures. The HVA requires time evolution generated by terms in the Hamiltonian. For the HAFM, this amounts to turning on an exchange interaction between qubits, which is native to quantum dot architectures [32–35]. In Sec. IV, we show this interaction can also be realized on the superconducting hardware by Google AI Quantum [36] using a single native two-qubit gate and at most four single-qubit gates. (If a two-qubit gate is equal to a single native gate up to single-qubit rotations, we call the former gate ‘essentially native’.)

Next to the HVA, a well-known type of ansatz is the Hardware-Efficient Ansatz (HEA) [12, 37]. The HEA is hardware-inspired; the circuit generating the ansatz state consists, by definition, of gates native to the hardware, avoiding the need to compile the ansatz into native gates. However, the HEA suffers from the ‘barren plateau’ problem: the gradient of the energy cost function is exponentially small in the number of parameters [38]. The HVA, on the other hand, is problem-inspired, and there is some evidence that it does not suffer from the barren plateau problem [39]. However, for execution on a quantum computer, gates in the HVA generally need to be compiled to gates native to that quantum computer. This increases the circuit depth, which is undesirable for NISQ devices. For KVQE<sub>G</sub>, such compilation is not required on quantum dot architectures, and only minimal compilation that does not increase the number of two-qubit gates is needed on Google’s hardware. So, to summarize, KVQE on quantum dot and Google’s superconducting hardware has the unique property that the HVA is essentially equal to the HEA.

Finally, KVQE<sub>G</sub> is close to NISQ hardware because it runs on hardware with the connectivity of a 2D grid with minimal overhead. This is the connectivity that is also required for the surface code [40], and therefore much effort is put into designing platforms with grid connectivity [16, 35, 41–43].

## B. Summary of numerical results

The task for KVQE<sub>G</sub> reported here is the simulation of a 20-site open patch of the kagome HAFM. For this

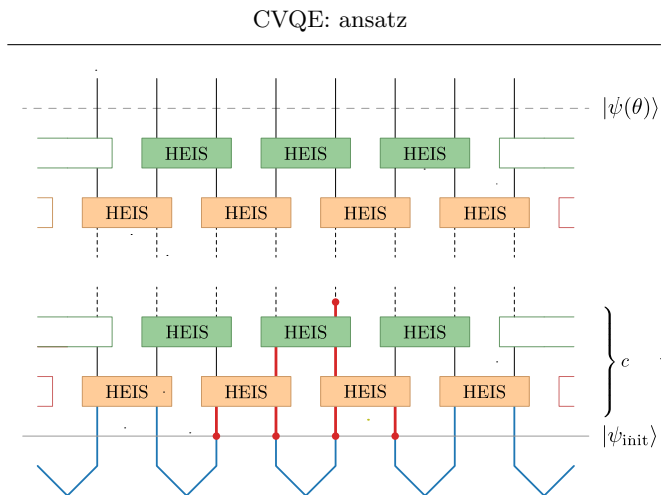


Figure 3. The ansatz for CVQE, with time running from bottom to top. The initial state  $|\psi_{\text{init}}\rangle$  consists of  $n/2$  adjacent singlets, displayed in blue. The circuit that is applied to  $|\psi_{\text{init}}\rangle$  consists of  $p$  repetitions of a cycle  $c$ , each time with new parameters, and with one parameter per gate. For one of the qubits, the past light cone (discussed in Sec. III B) that is due to a single cycle  $c$  (thus excluding the singlet generation) is displayed with thicker, red lines.

case, we assume a noiseless 24-qubit quantum computer with grid connectivity, the ability to natively implement the exchange interaction, SWAP,  $\sqrt{Z}$  and  $X$  gates, and where every exchange interaction gate in the ansatz circuit has its own parameter. We emulate this quantum computer classically, as is detailed in Sec. II D. The optimal state obtained by KVQE is compared to the exact ground state of the 20-site patch, which is obtained by exact diagonalization. We find that the optimal energy obtained by KVQE<sub>G</sub> approaches the true ground state energy exponentially as a function of the circuit depth. Also, the fidelity (overlap squared) between the optimal state and the true ground state approaches unity exponentially in the circuit depth. A fidelity of  $>99.9\%$  is reached at a circuit depth of 99. More detail is found in Fig. 4 and Sec. III A.

The task for KVQE<sub>K</sub> reported here is the simulation of an 18-site *periodic* patch. For this case, we assume a noiseless 18-qubit quantum computer with all-to-all connectivity, and the other settings as before [44]. The optimal energy obtained by KVQE<sub>G</sub> approaches the true ground state energy exponentially as a function of the circuit depth. The fidelity initially plateaus, but then continues exponentially towards unity. A fidelity of  $>99.9\%$  is reached at a circuit of depth 151. We find the increment of the circuit depth required for obtaining a fidelity of  $>99.9\%$  (as compared to the previous paragraph) not to be the result of the different ansatz, but rather to be the result of the difference in the systems that are simulated. More detail is found in Fig. 5 and Sec. III A.

Under the hardware assumptions of KVQE<sub>G</sub>, we let CVQE simulate a 20-site periodic chain. The fidelity

and energy of the optimal state found by CVQE improve exponentially as a function of circuit depth, with a sudden improvement of performance after  $p_{\text{crit}} = 5$  due to the availability of system-wide entanglement after  $p_{\text{crit}}$ . The optimal state found by CVQE reaches a fidelity of  $>99.9\%$  at a circuit of depth 19. More detail is found in Fig. 6 and Sec. III B.

## II. METHODS

### A. VQE

In this subsection, we give a more detailed introduction to VQEs. It may be skipped by readers already familiar with VQEs. The problem of finding the ground state energy of general  $k$ -local Hamiltonians is believed to be intractable even on quantum computers [45–47]. Nevertheless, there may be problem instance classes for which quantum computers could solve for the ground state efficiently. The Variational Quantum Eigensolver (VQE) is a proposed general method for finding ground states on quantum computers.

Consider a quantum mechanical system with Hilbert space  $\mathcal{H}$  of dimension  $N$ , Hamiltonian  $H$  with ground state energy  $E_0$ , and a subset of parametrized states  $\{|\theta\rangle\} \subseteq \mathcal{H}$ , with  $\theta \in \mathbb{R}^m$ . To describe all of  $\mathcal{H}$ , it is necessary that  $m = O(N)$ . The fact that

$$E(\theta) = \langle \theta | H | \theta \rangle \geq E_0$$

for all  $|\theta\rangle \in \mathcal{H}$  is called the variational principle. For reasons of scalability, in variational methods, one generally employs a set of states described by  $m = \text{polylog } N$  parameters. Variational methods, like the VQE, seek to minimize  $E(\theta)$  to hence establish an upper bound for the ground state energy.

As input, a VQE receives a description of a Hamiltonian on  $n$  spin-1/2 particles,

$$H = \sum_{i=1}^l h_i H_i, \quad (1)$$

with  $h_i$  real coefficients and  $H_i$  Hermitian operators. For  $k$ -local Hamiltonians,  $l = \text{poly } n$ .

A VQE proceeds by first choosing an initial set of parameters  $\theta$ . These initial parameters may be chosen at random or may be inspired by a classical approximate solution to the ground state, for example by the Hartree-Fock ground state [48]. Then, a criterion is chosen, for example, that a maximum number of iterations has not been reached, or that  $E(\theta)$  has not reached a value below a given threshold. The VQE then proceeds as follows.

1. While the criterion is true, repeat:

- (a) *Prepare the ansatz*  $|\theta\rangle$ .  
Prepare the initial state  $|\psi_{\text{init}}\rangle$ . Apply a parametrized circuit  $C(\theta)$  to obtain the state

### KVQE<sub>G</sub>: results

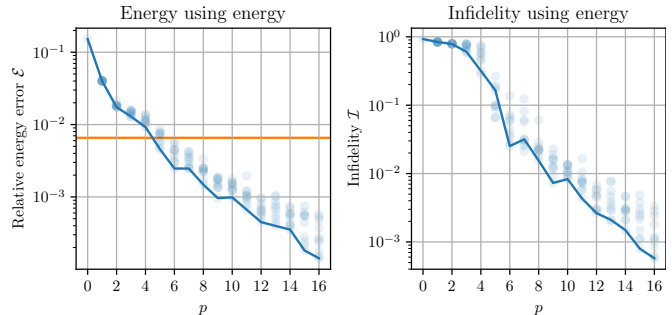


Figure 4. **(Left)** Semi-log plot of the relative energy error [Eq. (5)] obtained by KVQE for 20 sites (Fig. 2), as a function of the number of cycles  $p$ . Translucent points represent the 10 local minima that were found by KVQE per  $p$ . Every cycle is a circuit of depth 6 and uses 30 parameters. The solid line connects the lowest local minima  $E(\theta^*)$ . An orange horizontal line is drawn at the value of  $\mathcal{E}$  corresponding to the energy of the first excited state. **(Right)** Semi-log plot of the infidelities of the states corresponding to the local minima in the left plot. The solid line connects the points that, for a given  $p$ , are lowest in energy. Although it occurs regularly, these points need not have the lowest infidelity.

### KVQE<sub>K</sub>: results

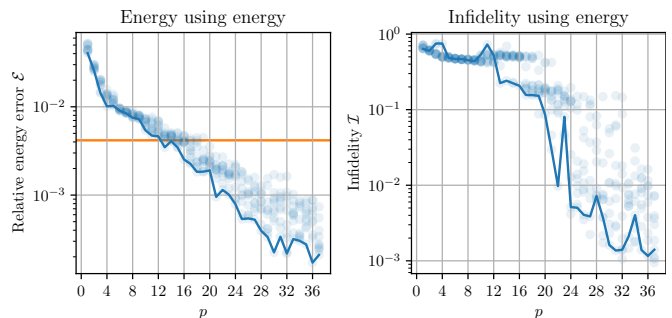


Figure 5. Semi-log plots similar to those in Fig. 4, but now for KVQE<sub>K</sub>, simulating a periodic patch of 18 sites (Fig. 1). Per  $p$ , ten local minima are displayed. Every cycle is a circuit of depth 4 and uses 36 parameters.

$|\theta\rangle = C(\theta)|\psi_{\text{init}}\rangle$ . The circuit  $C(\theta)$  usually consists of gates on fixed positions, where every or some of the gates are parametrized.

- (b) *Measure and store*  $E(\theta)$ .  
By linearity,  $E(\theta) = \sum_i h_i \langle \theta | H_i | \theta \rangle$ . Each expectation value  $\langle \theta | H_i | \theta \rangle$  can be estimated by measuring the operator  $H_i$  repeatedly (each measurement requires a new preparation of  $|\theta\rangle$ ) and taking the statistical average. See Ref. [11] for the expected number of measurements using this method, or Ref. [49], and references therein, for more efficient methods.
- (c) *Update*  $\theta$ .  
Based on  $E(\theta)$  and previous outcomes of  $E(\theta)$ ,

update  $\theta$  according to some classical optimization algorithm.

- Return  $\theta^*$ , which we define as the  $\theta$  that achieved the lowest energy.

Physically relevant information, such as correlation functions, can now be extracted from  $|\theta^*\rangle$  by repeatedly preparing and performing measurements on  $|\theta^*\rangle$ . Different VQEs differ in the way circuits are parametrized, how (an estimate for)  $E(\theta)$  is obtained, and what specific optimization routine is used. These will be detailed in the subsequent sections.

## B. Ansatz

### 1. Cyclic HVA

In the Hamiltonian Variational Ansatz (HVA) [20], the initial state  $|\psi_{\text{init}}\rangle$  is the ground state of a Hamiltonian  $H_{\text{init}}$ . The Hamiltonian  $H_{\text{init}}$  is chosen so that its ground state is known and easy to prepare. The ansatz state  $|\theta\rangle$  is obtained by sequentially evolving along terms in  $H$ , according to some fixed sequence  $i$ ,

$$|\theta\rangle = C(\theta)|\psi_{\text{init}}\rangle,$$

with

$$C(\theta) = \exp(-i\theta_M H_{i_M}) \dots \exp(-i\theta_2 H_{i_2}) \exp(-i\theta_1 H_{i_1}).$$

The  $M$  parameters are formed by the time duration of the  $M$  evolutions. Often, as for example in, but not limited to, Refs. [20, 21, 27, 39],  $C$  consists of  $p$  cycles of a smaller circuit  $c$ , each time defined by the same sequence  $i$  of terms in the Hamiltonian. Every cycle gets its own set of  $m$  parameters. It is convenient to write  $\theta$  as  $\theta = (\theta_1, \dots, \theta_p)$ , with  $\theta_j = (\theta_{j_1}, \dots, \theta_{j_m})$ . Then, a single cycle reads

$$c(\theta_j) = \exp(-i\theta_{j_m} H_{i_m}) \dots \exp(-i\theta_{j_2} H_{i_2}) \exp(-i\theta_{j_1} H_{i_1}),$$

and so

$$|\theta\rangle = c(\theta_p) \dots c(\theta_1) |\psi_{\text{init}}\rangle. \quad (2)$$

We call this type of HVA the *cyclic* HVA. The cyclic HVA shows a close relation between static quantum simulation and dynamic quantum simulation; choosing  $i = (1, \dots, l)$  (or a permutation thereof) and  $\theta_j = (t/p, \dots, t/p)$  for all  $j$ , the cyclic HVA implements quantum time evolution for a target time  $t$  with  $p$  Trotter steps. In this way, the cyclic HVA can also mimic (but is more general than) adiabatic time evolution. In the case that no gap closes while adiabatically evolving from  $H_{\text{init}}$  to  $H$ , the HVA thus ensures that the ground state of  $H$  can be prepared with the ansatz (but without guaranties on the required circuit depth). This formed the initial motivation for the HVA in VQEs [20].

## CVQE: results

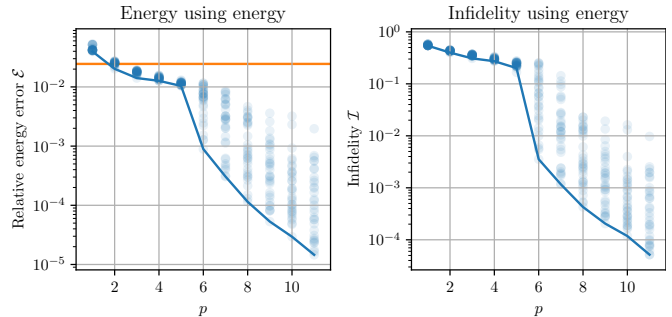


Figure 6. Semi-log plots similar to those in Fig. 4, but now for CVQE (Fig. 3), simulating the HAFM on a periodic chain of 20 sites. Per  $p$ , 32 local minima are displayed. Every cycle is a circuit of depth 2 and uses 20 parameters.

### 2. The HVA in this work

We use the cyclic HVA, where the Hamiltonian (in units where  $\hbar = 1$ ) is given by the HAFM Hamiltonian [cf. Eq. (1)]

$$H = \sum_{\langle i,j \rangle} \mathbf{S}^{(i)} \cdot \mathbf{S}^{(j)}, \quad (3)$$

where  $\mathbf{S}^{(i)} = (X_i, Y_i, Z_i)^T/2$  with  $X_i, Y_i, Z_i$  the Pauli matrices acting on spin  $i$  only, and where the sum runs over the edges  $\langle i, j \rangle$  of some graph  $G$ . In this work,  $G$  is either an open or periodic patch of the kagome lattice, or a periodic chain, and we take  $H_{\text{init}} = \sum_{\langle i,j \rangle'} \mathbf{S}^{(i)} \cdot \mathbf{S}^{(j)}$ , with  $\langle i, j \rangle'$  edges in a perfect matching of  $G$ . Since the ground state of a single term in  $H$  is the singlet state  $|s\rangle = (|01\rangle - |10\rangle)/\sqrt{2}$ , this means  $|\psi_{\text{init}}\rangle$  is a so-called dimer covering on the relevant physical system, where every dimer is a singlet state.

We define the gate HEIS as time evolution along a single term in the HAFM Hamiltonian. In the computational basis of two qubits, it reads

$$\begin{aligned} \text{HEIS}(\alpha) &\equiv e^{-i\alpha/4} e^{-i\alpha \mathbf{S}^{(1)} \cdot \mathbf{S}^{(2)}} \\ &= \begin{pmatrix} e^{-i\alpha/2} & 0 & 0 & 0 \\ 0 & \cos(\alpha/2) & -i\sin(\alpha/2) & 0 \\ 0 & -i\sin(\alpha/2) & \cos(\alpha/2) & 0 \\ 0 & 0 & 0 & e^{-i\alpha/2} \end{pmatrix}. \end{aligned} \quad (4)$$

In a parametrized circuit [Eq. (2)], every instance of the HEIS gate gets its own parameter  $\alpha = \theta_{j_k}$ .

### 3. Symmetry and the spin gap

The initial states, Hamiltonian, and circuits  $C$  we use in this work possess an  $SU(2)$  rotational symmetry [50]. For the two-spin singlet state  $|s\rangle$ , the total spin quantum number  $S$  and the total magnetization quantum number

$S_z$  vanish, and therefore  $S = S_z = 0$  for our initial states  $|\psi_{\text{init}}\rangle$ . By the  $SU(2)$  symmetry of  $C$ , also  $S = S_z = 0$  for  $|\theta\rangle$ . This reduces the search space of KVQE $_{G/K}$  and CVQE to the correct total spin sector [51].

The energy difference between the lowest energy eigenstate in the  $S = 0$  sector and the lowest energy eigenstate in the  $S = 1$  sector is known as the spin gap, or the singlet-triplet gap, and is of importance in describing the low-energy physics of the kagome HAFM [2, 5, 19, 52–54]. Similar to the ideas in Ref. [55], KVQE $_{G/K}$  and CVQE can be extended to study the spin gap by running them with an  $S = 1$  initial state, obtaining an optimal energy  $E(\theta_{S=1}^*)$ , in addition to running them with a  $S = 0$  dimer covering as the initial state, obtaining  $E(\theta_{S=0}^*)$ . An estimate for the spin-gap is then given by  $E(\theta_{S=1}^*) - E(\theta_{S=0}^*)$ .  $S = 1$  initial states can be obtained by changing one of the singlets in our  $|\psi_{\text{init}}\rangle$  into one of the three triplet states;  $|t_1\rangle = |00\rangle$ ,  $|t_0\rangle = \mathbf{S}_-^{(12)} |t_1\rangle / \sqrt{2} = (|01\rangle + |10\rangle) / \sqrt{2}$ , or  $|t_{-1}\rangle = \mathbf{S}_-^{(12)} \mathbf{S}_-^{(12)} |t_1\rangle / 2 = |11\rangle$ , with  $\mathbf{S}_\mp^{(12)} = \sum_{i=1}^2 \mathbf{S}_x^{(i)} \mp i \mathbf{S}_y^{(i)}$  the lowering (raising) operator on two qubits. Thus, we obtain a  $(S = 1, S_z = 1)$ ,  $(S = 1, S_z = 0)$ , or  $(S = 1, S_z = -1)$  dimer covering as the initial state, respectively. Because of the  $SU(2)$  symmetry of any  $(S = 0, S_z = 0)$  dimer covering, of  $C$ , and of  $H$ , the energy  $E(\theta)$  is invariant under the choice of triplet state as long as the symmetry is not broken by the (noisy) hardware. To see this, change the first singlet of the dimer covering  $|\psi_{\text{init}}\rangle$  into any of the singlet states, and denote the remainder of the initial state, which is a  $(S = 0, S_z = 0)$  dimer covering on  $n-2$  qubits, by  $|\text{dim}\rangle$ . Thus, we obtain the initial state  $2^{-m/2} [\mathbf{S}_-^{(12)}]^m |t_1\rangle |\text{dim}\rangle$ . Denote the lowering (raising) operator acting on all qubits by  $\mathbf{S}_\mp^{(\text{tot})} = \sum_{i=1}^n \mathbf{S}_x^{(i)} \mp i \mathbf{S}_y^{(i)}$ , and note  $\mathbf{S}_\mp^{(12)\dagger} = \mathbf{S}_\pm^{(12)}$ ,  $\mathbf{S}_\mp^{(\text{tot})\dagger} = \mathbf{S}_\pm^{(\text{tot})}$ . Then,

$$\begin{aligned} E(\theta) &= 2^{-m} \langle t_1 | [\mathbf{S}_+^{(12)}]^m \langle \text{dim} | C^\dagger H C [\mathbf{S}_-^{(12)}]^m | t_1 \rangle |\text{dim}\rangle \\ &= 2^{-m} \langle t_1 | \langle \text{dim} | [\mathbf{S}_+^{(\text{tot})}]^m C^\dagger H C [\mathbf{S}_-^{(\text{tot})}]^m | t_1 \rangle |\text{dim}\rangle \\ &= \langle t_1 | \langle \text{dim} | C^\dagger H C | t_1 \rangle |\text{dim}\rangle, \end{aligned}$$

which does not depend on  $m \in \{0, 1, 2\}$ .

Under the influence of noise, the circuit  $C(\theta)$  will generally not produce a pure state  $|\theta\rangle$ , but rather a mixed state  $\rho_\theta$ . If the noise breaks the  $SU(2)$  symmetry of  $C$ , KVQE $_{G/K}$  and CVQE (running with  $S = 1$  initial states) may abuse this noise to put amplitude on  $S = 0$  states, thus obtaining unjustly low variational energies. This may be dealt with by symmetry verification [56]. Alternatively, a penalty term  $A_{P_1} (\mathbf{S}^2 - 2)^2$ , with  $A_{P_1} > 0$ , may be added to  $H$ . In the Pauli basis, this penalty term has  $O(n^4)$  terms, and may hence be too costly to compute in every iteration of KVQE $_{G/K}$  and CVQE. A more efficient option is to start in the initial state  $|t_1\rangle |\text{dim}\rangle$ , using the penalty term  $A_{P_2} (\mathbf{S}_z - 1)^2$ , with  $\mathbf{S}_z$  the total spin in the  $z$ -direction and  $A_{P_2} > 0$ . This penalizes having ampli-

tude on states (within the ansatz state) that have  $S_z \neq 1$ . This means a penalty on all  $S = 0$  states since  $S_z = 0$  for all  $S = 0$  states. In the remainder of this work, we focus on  $S = 0$  initial states for numerical emulation and leave the study of the performance of KVQE $_{G/K}$  and CVQE using  $S = 1$  initial states for future work.

#### 4. Parameter multiplicity

In this paper, every Heisenberg gate in the ansatz gets its own parameter; we have One parameter Per Gate (OPG). Another possibility would be to have multiple HEIS gates per cycle share the same parameter. We call this One parameter Per Slice (OPS). We say the qubits sharing the same parameter are in the same ‘slice’.

A possible advantage of OPS is that, by choosing proper slices, we can ensure that the state produced by the circuit has the lattice symmetries expected to be present in the ground state. This would make the search space smaller by only restricting to states with the desired lattice symmetry.

Nevertheless, OPG has advantages over OPS. With OPS, we may overlook symmetry broken ground states. For example, it is unknown whether the ground state of the kagome lattice has a spontaneously broken symmetry [5]. Secondly, even if the ground state does not break any symmetries, the depth of the OPG circuit for a given state may be lower than the depth of the OPS circuit that produces the same state. For NISQ devices, it is imperative to keep circuit depths as low as possible. Finally, the inherent noise-resilience of VQEs may be compromised by choosing OPS over OPG. As an illustration, say we are given a noiseless quantum computer, a Hamiltonian and a minimal-depth OPS circuit that produces the ground state of that Hamiltonian. Suppose that now a static but random over-rotation is added to each HEIS gate. Then it is very unlikely that the OPS circuit can still produce the correct ground state, no matter its parameters. When we lift the restriction that the gates in every slice share the same parameter, and hence go to an OPG circuit, the over-rotations can be absorbed into the parameters, and hence the ground state can still be produced without an increase in circuit depth.

### C. Analysis

We assess the effectiveness of KVQE $_{G/K}$  and CVQE by running them for fixed system sizes but a varying number of cycles  $p$ . For every  $p$ , we plot the relative energy error  $\mathcal{E}$  between the true ground state energy,  $E_0$ , and the optimal energy found by the VQE,  $E(\theta^*)$ ,

$$\mathcal{E} = \left| \frac{E(\theta^*) - E_0}{E_0} \right|. \quad (5)$$

Additionally, we plot the infidelity  $\mathcal{I}$  between the true ground state  $|E_0\rangle$  and the optimal state obtained by the

VQE,  $|\theta^*\rangle$ ,

$$\mathcal{I} = 1 - \mathcal{F} \equiv 1 - |\langle E_0 | \theta^* \rangle|^2,$$

with  $\mathcal{F}$  the fidelity between  $|E_0\rangle$  and  $|\theta^*\rangle$ . Even in plots showing the infidelity, the corresponding VQE optimized the energy, not the infidelity. The infidelity is a useful figure of merit because it upper bounds the relative error in expectation value of any observable [57],

$$\frac{|\langle E_0 | O | E_0 \rangle - \langle \theta^* | O | \theta^* \rangle|}{\|O\|} \leq 4\sqrt{\mathcal{I}},$$

with  $\|\cdot\|$  the operator norm.

We obtain  $E_0$  and  $|E_0\rangle$ , and thus  $\mathcal{E}$  and  $\mathcal{I}$ , by exact diagonalization. For large system sizes, such as those needed for obtaining a quantum advantage, this will no longer be possible.

#### D. Classical implementation

We emulate the quantum circuits in this work using the home-grown, optionally GPU-accelerated, classical quantum emulator `HeisenbergVQE`. Documentation, source code and all generated data is available as Supplementary Material [18]. `HeisenbergVQE` is tailored to running VQEs for the Heisenberg model on any graph. It is written in Python [58], with performance-critical code delegated to C via NumPy [59] if GPU acceleration is off, and CUDA via CuPy [60] if GPU acceleration is on.

We exploit the full access to the wave function, granted by classical emulation, in the computation of  $E(\theta)$ . We assume a noiseless quantum computer and use a gradient-based optimization method. Gradients are computed using backward-mode automatic differentiation [61], as implemented in Chainer [62].

For optimization of the cost function  $E(\theta)$ , we first choose initial parameters uniformly at random in the interval  $[-10^{-3}, 10^{-3}]$ . There is some evidence that for the HVA, points close to the origin in parameter space are good starting points for local optimization [39]. We then use the BFGS algorithm, as implemented in SciPy [63], to find a local minimum. At every step of the BFGS routine, the energy and the gradient of the energy are calculated. Here, we call these two steps together one *function call*. The steps of random parameter generation and local optimization (one ‘round’) are repeated a variable number of times. The parameters that achieve the lowest energy out of all local minimization rounds,  $\theta^*$ , are stored together with  $E(\theta^*)$ . Starting many rounds of local optimization from unrelated starting points has the benefit of straightforward parallelization.

`HeisenbergVQE` computes exact ground states using SciPy’s wrapper of ARPACK, which implements the Implicitly Restarted Lanczos Method [64]. Operator-vector multiplication is optionally GPU accelerated. The energy of the exact ground state and the exact ground state vector itself are used as a reference for the performance of the

VQEs in this work. Such reference will not be available for system sizes used in experiments showing a quantum advantage.

The Supplementary Material [18] also includes data and plots for systems and ansätze not reported in this work, including simulations of the HAFM on the triangular lattice, other system sizes of the kagome lattice, simulations that use one parameter per slice (see Sec. II B), `KVQEG` simulating periodic patches, `KVQEK` simulating open patches, and runs where we use the infidelity as the cost function. Using the infidelity as a cost function is impractical on quantum computers (or even impossible if the ground state is not known), but may be used by classical computers to obtain further data on the expressibility of an ansatz. For all systems, data were stored in a human-readable format, and include the number of calls to the cost function by the BFGS routine, the wall-clock time of the classical emulation, the initial parameters, and the parameters, energy, and infidelity of the local minima.

### III. NUMERICAL RESULTS AND ANALYSIS

#### A. Kagome

The explicit initial state and circuit used by `KVQEG` for the simulation of the HAFM on a 20-site patch of the kagome lattice is depicted in Fig. 2. For this patch, `KVQEG` uses 20 data qubits to represent the 20 sites of the patch, and an additional 4 qubits as ‘swapping stations’, used to realize kagome connectivity on grid architectures. The restriction of grid connectivity increases the circuit depth per cycle (assuming HEIS gates are native) from 4 to 6, and (in the thermodynamic limit) introduces one auxiliary qubit per three qubits. Because every gate gets its own parameter, the total number of parameters is  $M = 30p$ .

Results are displayed in Fig. 4. The relative energy error  $\mathcal{E}$  decreases roughly exponentially in the range of all considered  $p$ . The number of function calls scales polynomially with  $p$  (data available at [18]). `KVQEG` finds an energy lower than the energy of the first excited state for  $p \geq 5$ . There is no clear critical  $p$  after which  $\mathcal{E}$  and/or  $\mathcal{I}$  improve drastically. Nevertheless,  $\mathcal{I}$  transitions to an improved exponential decay rate somewhere between  $p = 3$  and  $p = 5$ , reaching a fidelity of  $>99.9\%$  at  $p \geq 16$ . Under the hardware assumptions of subsection (Sec. IB),  $p = 16$  amounts to  $20/2 \times 3 = 30$  gates for the generation of the singlets,  $30 \times 16 = 480$  HEIS gates, and  $16 \times 16 = 256$  SWAP gates, giving a total of 766 gates and 480 parameters. The total depth equals  $3 + 6 \times 16 = 99$ . To obtain the 10 local minima at  $p = 16$  a total of 82,466 function calls were made.

The explicit initial state and circuit used by `KVQEK` for the simulation of an 18-site periodic patch are depicted in Fig. 1. For this patch, we assume a noiseless quantum computer with 18 qubits and all-to-all connec-

tivity. Results for  $\text{KVQE}_K$  are displayed in Fig. 5. Again,  $\mathcal{E}$  decreases roughly exponentially in the range of all considered  $p$ , whereas the number of function calls scales polynomially with  $p$  [18].  $\text{KVQE}_K$  finds an energy lower than the energy of the first excited state for  $p \geq 13$ . After that same  $p$ , the performance of  $\mathcal{I}$  improves significantly.

We note that for  $p$  such that the ansatz is not expressive enough to attain energies below the first excited state (in the present case, this is for  $p < 13$ ), there need not be a relation between the energy of an ansatz state and its overlap with the ground state; in this regime, the ansatz may, for example, prepare states with large overlap with the first excited state, and zero overlap with the ground state. It is only for  $p$  such that the ansatz can reach energies below the first excited state that a decrease in energy must be met with a decrease in infidelity. Data obtained using the infidelity as the cost function does show uniform exponential decay of  $\mathcal{I}(p)$  [18].

$\text{KVQE}_K$  (using the energy as the cost function) reaches a fidelity of  $>99.9\%$  at  $p \geq 37$ . Under the hardware assumptions of subsection (Sec. IB),  $p = 37$  amounts to  $18/2 \times 3 = 27$  gates for the generation of the singlets,  $36 \times 37 = 1332$  HEIS gates, giving a total of 1359 gates and 1332 parameters. The total depth equals  $3 + 4 \times 37 = 151$ . To obtain the 10 local minima at  $p = 37$ , a total of 191,582 function calls were made.

One striking feature of these results is that the rate of exponential decay of the optimal energy and infidelity as a function of the number of cycles  $p$  is significantly smaller (in absolute value) than those same rates obtained by  $\text{KVQE}_G$ . This difference in performance is not because of the difference in the structure of the ansatz, but because of the difference in the systems being simulated; the performance of  $\text{KVQE}_G$  in simulating the periodic patch of Fig. 1 (in this case the ansatz for  $\text{KVQE}_G$  is obtained by extending the ansatz of Fig. 2 so that its effective HEIS gates cover the periodic patch of Fig. 1), does not differ significantly from the performance of  $\text{KVQE}_K$  on that same patch [18]. Vice versa, the performance of  $\text{KVQE}_K$  (in this case the ansatz for  $\text{KVQE}_K$  is obtained by extending the ansatz of Fig. 1 so that its effective HEIS gates cover the open patch of Fig. 2) in simulating the 20-site open patch of Fig. 2 (top right) does not differ significantly from the performance of  $\text{KVQE}_K$  on that same patch [18].

At first, the 18-site periodic patch of Fig. 1 might seem to be easier to simulate than the 20-site open patch of Fig. 2 (top right) because of the difference in the number of sites. However, the graph defining the periodic patch has 36 edges, as opposed to 30 edges for the open patch. Therefore, the optimization problem corresponding to the open patch has more ‘constraints’, and can therefore naturally be more challenging. Additionally, boundary effects, which are absent in the periodic patch, may lead to a ground state that is easier to prepare. We leave an investigation of the latter issue for further work.

## B. Chain

The explicit initial state and circuit used by CVQE for the simulation of a 20-site periodic chain are depicted in Fig. 3. Any Quantum Processing Unit (QPU) with grid, kagome, or all-to-all connectivity naturally embeds subsets of qubits with (at least) the connectivity of a periodic chain. Because every gate gets its own parameter, the total number of parameters is  $M = 20p$ .

Results are displayed in Fig. 6. Both the relative energy error  $\mathcal{E}$  and the infidelity  $\mathcal{I}$  (Sec. IIC) initially decrease exponentially as a function of  $p$ , reaching an energy that is below the first excited state for  $p \geq 2$ . Both functions show a sudden improvement after  $p_{\text{crit}} = 5$ . From  $p_{\text{crit}}$  to  $p_{\text{crit}} + 1$ ,  $\mathcal{E}$  drops by an order of magnitude, and  $\mathcal{I}$  drops by two orders of magnitude. For  $p > 5$ , both functions again decrease roughly exponentially with a rate that is greater in magnitude than before. At the same time, the number of function calls (as defined in Sec. IID, data not shown in the plot but available at [18]) grows polynomially with  $p$ . A fidelity of  $>99.9\%$  is reached for  $p \geq 8$ . Assuming HEIS gates are native, and that singlets can be created with a circuit of depth 3 (Appendix IV),  $p = 8$  amounts to a circuit with  $20/2 \times 3 = 30$  gates for the preparation of singlets and  $20 \times 8 = 160$  HEIS gates, giving a total of 190 gates and 160 parameters. The depth of the circuit is  $3 + 8 \times 2 = 19$ . The optimization routine for finding the 32 local minima at  $p = 8$  used 104,890 function calls. A fidelity of  $>99.99\%$  is reached at  $p = 11$  cycles, using a total of 197,685 function calls.

A plausible explanation of the sudden improvement of CVQE beyond  $p_{\text{crit}} = 5$  is in terms of the past light cone. The past light cone of a qubit  $q$  after a circuit  $C$  consists of all qubits  $q'$  for which there exists a past-directed path through  $C$  that connects  $q$  to  $q'$ . It is only when  $q'$  is in the past light cone of  $q$  that  $C$  can build up entanglement between  $q$  and  $q'$ . Also see Fig. 3. The ground state of the HAFM on the chain is known to possess long-range entanglement [65]. The sudden improvement of performance is a clear sign of a ground state with long-range entanglement. At  $p_{\text{crit}}$ , there is no qubit whose past light cone at the end of  $C$  covers the entire chain. After  $p_{\text{crit}}$ , the past light cone of *every* qubit at the end of  $C$  covers the entire chain.

For  $\text{KVQE}_G$  not all qubits’ past light cones cover the entire system for the first time at an identical number of cycles [66]. For  $\text{KVQE}_K$ , the past light cone of every qubit covers the entire patch for the first time at  $p = 3$ . However, unlike CVQE, the states that can be reached by  $\text{KVQE}_K$  at this depth are still very far from the true ground state, and no sudden improvement of performance is observed.

The data available at [18] admits a detailed finite-size study of the circuit depth needed to obtain a given target fidelity as a function of the length of the chain. We leave this for future work.

#### IV. QUANTUM HARDWARE IMPLEMENTATION

The HEIS gate is directly native to quantum dot architectures. This also allows native implementation of the SWAP gate on these devices since  $\text{SWAP} = i \text{HEIS}(\pi)$ .

The native, parametrized two-body gate of Google AI Quantum equals [36]

$$\text{fSim}(\theta, \phi) = \begin{pmatrix} 1 & 0 & 0 & 0 \\ 0 & \cos(\theta) & -i \sin(\theta) & 0 \\ 0 & -i \sin(\theta) & \cos(\theta) & 0 \\ 0 & 0 & 0 & e^{-i\phi} \end{pmatrix}.$$

The HEIS gate is periodic, up to an overall phase, with period  $2\pi$ . For  $-\pi \leq \alpha < \pi$ , the fSim gate is related to the HEIS gate by

$$\text{HEIS}(\alpha) = \text{RZ}_0(\alpha/2)\text{RZ}_1(\alpha/2)\text{fSim}(\alpha/2, \alpha), \quad (6)$$

with  $\text{RZ}_0(\theta) = \text{RZ}(\theta) \otimes \mathbb{1}$  and  $\text{RZ}_1(\theta) = \mathbb{1} \otimes \text{RZ}(\theta)$ , where  $\text{RZ}(\theta) = e^{-i\theta Z/2}$ , and  $Z$  is the Pauli- $Z$  operator. According to Eq. (6), for  $0 \leq \alpha/2 \leq \pi/2$ , a  $\text{HEIS}(\alpha)$  gate can be directly implemented using two single-qubit RZ gates and one fSim gate. For parameter values that fall outside that range, the following identities can be used,

$$\text{fSim}(\theta, \phi) = \begin{cases} Z_0 Z_1 \text{fSim}(\theta - \pi, \phi) & : -\pi \leq \theta < -\pi/2 \\ Z_0 \text{fSim}(-\theta, \phi) Z_0 & : -\pi/2 \leq \theta < 0 \\ \text{fSim}(\theta, \phi) & : 0 \leq \theta < \pi/2 \\ Z_0 \text{fSim}(-\theta + \pi, \phi) Z_1 & : \pi/2 \leq \theta < \pi \end{cases}.$$

Here,  $Z_0 = Z \otimes \mathbb{1}$  and  $Z_1 = \mathbb{1} \otimes Z$ .

The SWAP gate is related to the fSim gate by

$$\text{SWAP} = \sqrt{Z_0} \sqrt{Z_1} \text{fSim}(\pi/2, \pi).$$

The fSim gate in this equation can be implemented directly. Hence, a SWAP gate can be implemented by using one layer of RZ rotations and a single fSim gate. Assuming arbitrary single-qubit rotations are native, and a Heisenberg or fSim gate is native, singlets can be created between two adjacent qubits with a circuit of depth 3 (see Fig. 8).

By adding the angles of subsequent RZ rotations,  $\ell$  layers of HEIS and/or SWAP gates can be implemented by at most  $\ell$  layers of single-qubit RZ rotations and  $\ell + 1$  layers of fSim gates. Depending on the specific circuit, further reductions may be possible by using that  $\text{RZ}_0(\beta)\text{RZ}_1(\beta)$  commutes with  $\text{fSim}(\theta, \phi)$  and addition of RZ rotation angles. For an example, see Fig. 7.

#### V. DISCUSSION AND OUTLOOK

Current hardware does not yet simultaneously have grid connectivity (for more than 4 qubits) and the ability to essentially natively implement the exchange interaction for all parameter values. Quantum dot architectures

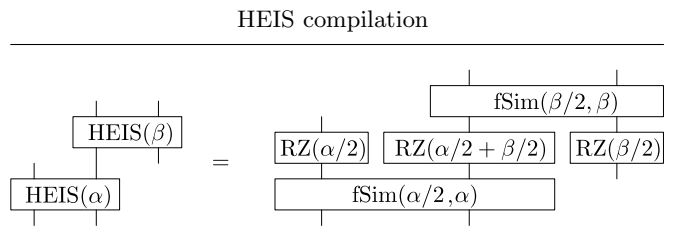


Figure 7. Example of the compilation of HEIS gates into fSim gates and single-qubit RZ rotations for  $0 \leq \alpha/2 \leq \pi$ .

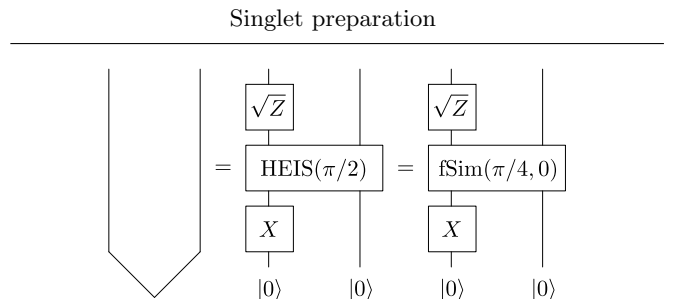


Figure 8. Circuits for preparing the singlet state up to a global phase (left), using gates native to quantum dots (middle) and Google's superconducting hardware (right).

can natively implement the exchange interaction but are not yet available with grid connectivity. However, this connectivity may become available in the future, as detailed proposals already exist [32, 33, 35, 67]. Google AI Quantum can implement the exchange interaction essentially natively for all parameter values (see Sec. IV) and can demonstrate grid connectivity [16], but is not yet able to combine these two features in a single processor. This has, however, been expressed as a future goal. (See Sec. C. of the Supplementary Material of Ref. [16].) They are already able to implement any two-qubit gate (so including the HEIS gate for all parameter values) using three native two-qubit gates [68]. Current hardware is already capable of efficiently performing CVQE for small problem sizes of open [36] or closed chains [35]. In such experiments, the observation of a critical circuit depth could form an early goal and would indicate the ability to generate and find ground states with system-wide entanglement.

For showing a quantum advantage with  $\text{KVQE}_G$  on a quantum computer, it is a prerequisite that it is first able to run  $\text{KVQE}_G$  for a 20-site patch of the kagome lattice. In this work, we have set a performance baseline for this patch; we do not expect a quantum computer to perform as well as the noiseless emulations in this work. How well a given quantum computer can approach this baseline forms an assessment of its capabilities and prospects. In such experiments, the extent to which the exponential decay rate of the relative energy error as a function of the number of cycles matches the decay rate presented in the current work, and the value of the relative energy

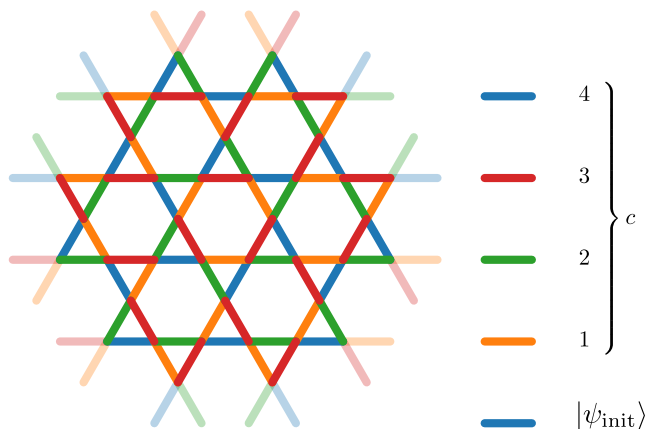
KVQE'<sub>K</sub>: ansatz

Figure 9. (Colour online.) One unit cell of a four-colouring of the kagome lattice (opaque edges), derived from the 36-site VBC (blue lines) of Refs. [6–10]. To four-colour the entire lattice using this unit cell, a hexagonal tiling of these unit cells needs to be made. This four-colouring directly translates to an ansatz for KVQE'<sub>K</sub>. On quantum computers with grid connectivity, we propose to use the same initial state, but define the cycle  $c$  similarly to the cycle defined for KVQE<sub>G</sub> defined in Fig. 2.

error at which the experimental VQE saturates, provide important performance characteristics. (We see no such saturation in the noiseless classical emulation, but it is expected to occur on noisy hardware.)

We expect KVQE'<sub>G/K</sub> for patches of more than 20 sites to also show an exponential decay of the relative energy

error as a function of the number of cycles. Due to the inherent limitations of classical emulation, a fully-fledged system-size scaling study of the rate of this exponential decay is outside the scope of the current work. Further investigation, possibly on real quantum devices, is needed to show how the rate of exponential decay changes with system size and noise levels.

In Refs. [6–10], the proposed ground state of the kagome HAFM is a 36-site VBC. We propose to use this VBC as the initial VQE state on quantum computers with at least that same number of data qubits. For large patches, this has the potential to answer whether this VBC is the ground state with very low circuit depths.

**Note added.** Shortly after the preprint of this paper was made public, an independent but similar work appeared by Bosse and Montanaro [69]. At a high level, Bosse and Montanaro’s work share the same motivation, methods and results as the current work. Differences include the exact mapping from the kagome lattice to a grid, the numerical implementation, and the simulated patches of the kagome lattice. In addition, Bosse and Montanaro report a preliminary finite-size scaling, data on the extraction of observables, and an investigation of the barren-plateau problem [38], where we include an ansatz for quantum computers with kagome connectivity and focus more on the experimental realization.

### Acknowledgements

The authors thank C.J. van Diepen, K.L. Groenland and P.R. Corboz for useful discussion. The numerical simulations in this work were carried out on the quantum simulation nodes of the Lisa cluster, provided by the Dutch national e-infrastructure with the support of SURF Cooperative.

- 
- [1] Hong-Chen Jiang, Zheng-Yu Weng, and Donna N Sheng, “Density matrix renormalization group numerical study of the kagome antiferromagnet,” *Physical Review Letters* **101**, 117203 (2008).
  - [2] Simeng Yan, David A Huse, and Steven R White, “Spin-liquid ground state of the  $s=1/2$  kagome heisenberg antiferromagnet,” *Science* **332**, 1173–1176 (2011).
  - [3] Philip W Anderson, “Resonating valence bonds: A new kind of insulator?” *Materials Research Bulletin* **8**, 153–160 (1973).
  - [4] M. R. Norman, “Colloquium : Herbertsmithite and the search for the quantum spin liquid,” *Reviews of Modern Physics* **88** (2016), 10.1103/revmodphys.88.041002.
  - [5] Andreas M Läuchli, Julien Sudan, and Roderich Moessner, “ $S=1/2$  kagome heisenberg antiferromagnet revisited,” *Physical Review B* **100**, 155142 (2019).
  - [6] JB Marston and C Zeng, “Spin-peierls and spin-liquid phases of kagomé quantum antiferromagnets,” *Journal of Applied Physics* **69**, 5962–5964 (1991).
  - [7] P Nikolic and T Senthil, “Physics of low-energy singlet states of the kagome lattice quantum heisenberg antiferromagnet,” *Physical Review B* **68**, 214415 (2003).
  - [8] Rajiv RP Singh and David A Huse, “Ground state of the spin-1/2 kagome-lattice heisenberg antiferromagnet,” *Physical Review B* **76**, 180407 (2007).
  - [9] Rajiv RP Singh and David A Huse, “Triplet and singlet excitations in the valence bond crystal phase of the kagome lattice heisenberg model,” *Physical Review B* **77**, 144415 (2008).
  - [10] Glen Evenbly and Guifr Vidal, “Frustrated antiferromagnets with entanglement renormalization: Ground state of the spin-1 2 heisenberg model on a kagome lattice,” *Physical Review Letters* **104**, 187203 (2010).
  - [11] Jarrod R McClean, Jonathan Romero, Ryan Babbush, and Alán Aspuru-Guzik, “The theory of variational hybrid quantum-classical algorithms,” *New Journal of Physics* **18**, 023023 (2016).
  - [12] Alberto Peruzzo, Jarrod McClean, Peter Shadbolt, Man-Hong Yung, Xiao-Qi Zhou, Peter J Love, Alán Aspuru-

- Guzik, and Jeremy L O'brien, "A variational eigenvalue solver on a photonic quantum processor," *Nature communications* **5**, 1–7 (2014).
- [13] John Preskill, "Quantum Computing in the NISQ era and beyond," *Quantum* **2**, 79 (2018).
- [14] Peter JJ O'Malley, Ryan Babbush, Ian D Kivlichan, Jonathan Romero, Jarrod R McClean, Rami Barends, Julian Kelly, Pedram Roushan, Andrew Tranter, Nan Ding, *et al.*, "Scalable quantum simulation of molecular energies," *Physical Review X* **6**, 031007 (2016).
- [15] Jan-Michael Reiner, Frank Wilhelm-Mauch, Gerd Schön, and Michael Marthaler, "Finding the ground state of the hubbard model by variational methods on a quantum computer with gate errors," *Quantum Science and Technology* **4**, 035005 (2019).
- [16] Frank Arute *et al.*, "Quantum supremacy using a programmable superconducting processor," *Nature* **574**, 505–510 (2019).
- [17] Han-Sen Zhong, Hui Wang, Yu-Hao Deng, Ming-Cheng Chen, Li-Chao Peng, Yi-Han Luo, Jian Qin, Dian Wu, Xing Ding, Yi Hu, *et al.*, "Quantum computational advantage using photons," *Science* **370**, 1460–1463 (2020).
- [18] See Supplemental Material at [URL will be inserted by publisher] for all data reported in this paper, the code that generated it, and additional data.
- [19] Andreas M. Läuchli, Julien Sudan, and Erik S. Sørensen, "Ground-state energy and spin gap of spin- $\frac{1}{2}$  kagomé-heisenberg antiferromagnetic clusters: Large-scale exact diagonalization results," *Phys. Rev. B* **83**, 212401 (2011).
- [20] Dave Wecker, Matthew B Hastings, and Matthias Troyer, "Progress towards practical quantum variational algorithms," *Physical Review A* **92**, 042303 (2015).
- [21] Wen Wei Ho and Timothy H. Hsieh, "Efficient variational simulation of non-trivial quantum states," *SciPost Phys.* **6**, 29 (2019).
- [22] Hans Bethe, "Zur theorie der metalle," *Zeitschrift für Physik* **71**, 205–226 (1931).
- [23] Fabio Franchini, *An Introduction to Integrable Techniques for One-Dimensional Quantum Systems* (Springer International Publishing, 2017).
- [24] Jean-Sébastien Caux, "Correlation functions of integrable models: A description of the ABACUS algorithm," *Journal of Mathematical Physics* **50**, 095214 (2009).
- [25] Daniel Stilck Franca and Raul Garcia-Patron, "Limitations of optimization algorithms on noisy quantum devices," (2020), [arXiv:2009.05532 \[quant-ph\]](https://arxiv.org/abs/2009.05532).
- [26] Harper R Grimsley, Sophia E Economou, Edwin Barnes, and Nicholas J Mayhall, "An adaptive variational algorithm for exact molecular simulations on a quantum computer," *Nature communications* **10**, 1–9 (2019).
- [27] Chris Cade, Lana Mineh, Ashley Montanaro, and Stasja Stanisic, "Strategies for solving the fermi-hubbard model on near-term quantum computers," *Physical Review B* **102**, 235122 (2020).
- [28] Frank Arute, Kunal Arya, Ryan Babbush, Dave Bacon, Joseph C. Bardin, Rami Barends, Andreas Bengtsson, Sergio Boixo, Michael Broughton, Bob B. Buckley, David A. Buell, Brian Burkett, Nicholas Bushnell, Yu Chen, Zijun Chen, Yu-An Chen, Ben Chiaro, Roberto Collins, Stephen J. Cotton, William Courtney, Sean Demura, Alan Derk, Andrew Dunsworth, Daniel Eppens, Thomas Eickl, Catherine Erickson, Edward Farhi, Austin Fowler, Brooks Foxen, Craig Gidney, Marissa Giustina, Rob Graff, Jonathan A. Gross, Steve Habegger, Matthew P. Harrigan, Alan Ho, Sabrina Hong, Trent Huang, William Huggins, Lev B. Ioffe, Sergei V. Isakov, Evan Jeffrey, Zhang Jiang, Cody Jones, Dvir Kafri, Kostyantyn Kechedzhi, Julian Kelly, Seon Kim, Paul V. Klimov, Alexander N. Korotkov, Fedor Kostritsa, David Landhuis, Pavel Laptev, Mike Lindmark, Erik Lucero, Michael Marthaler, Orion Martin, John M. Martinis, Anika Marusczyk, Sam McArdle, Jarrod R. McClean, Trevor McCourt, Matt McEwen, Anthony Megrant, Carlos Mejuto-Zaera, Xiao Mi, Masoud Mohseni, Wojciech Mruzekiewicz, Josh Mutus, Ofer Naaman, Matthew Neeley, Charles Neill, Hartmut Neven, Michael Newman, Murphy Yuezhen Niu, Thomas E. O'Brien, Eric Ostby, Bálint Pató, Andre Petukhov, Harald Putterman, Chris Quintana, Jan-Michael Reiner, Pedram Roushan, Nicholas C. Rubin, Daniel Sank, Kevin J. Satzinger, Vadim Smelyanskiy, Doug Strain, Kevin J. Sung, Peter Schmitteckert, Marco Szalay, Norm M. Tubman, Amit Vainsencher, Theodore White, Nicolas Vogt, Z. Jamie Yao, Ping Yeh, Adam Zalcman, and Sebastian Zanker, "Observation of separated dynamics of charge and spin in the fermi-hubbard model," (2020), [arXiv:2010.07965 \[quant-ph\]](https://arxiv.org/abs/2010.07965).
- [29] Michael A Nielsen *et al.*, "The fermionic canonical commutation relations and the jordan-wigner transform," *School of Physical Sciences, The University of Queensland* **59** (2005).
- [30] Sergey B Bravyi and Alexei Yu Kitaev, "Fermionic quantum computation," *Annals of Physics* **298**, 210–226 (2002).
- [31] Zhang Jiang, Amir Kalev, Wojciech Mruzekiewicz, and Hartmut Neven, "Optimal fermion-to-qubit mapping via ternary trees with applications to reduced quantum states learning," *Quantum* **4**, 276 (2020).
- [32] C. J. van Diepen, T. K. Hsiao, U. Mukhopadhyay, C. Reichl, W. Wegscheider, and L. M. K. Vandersypen, "Quantum simulation of antiferromagnetic heisenberg chain with gate-defined quantum dots," (2021), [arXiv:2103.08238 \[cond-mat.mes-hall\]](https://arxiv.org/abs/2103.08238).
- [33] Pierre Barthelemy and L. M. K. Vandersypen, "Quantum dot systems: a versatile platform for quantum simulations," *Annalen der Physik* **525**, 808–826 (2013).
- [34] Daniel Loss and David P DiVincenzo, "Quantum computation with quantum dots," *Physical Review A* **57**, 120 (1998).
- [35] Nico W Hendrickx, William IL Lawrie, Maximilian Russ, Floor van Riggelen, Sander L de Snoo, Raymond N Schouten, Amir Sammak, Giordano Scappucci, and Menno Veldhorst, "A four-qubit germanium quantum processor," *Nature* **591**, 580–585 (2021).
- [36] Brooks Foxen, Charles Neill, Andrew Dunsworth, Pedram Roushan, Ben Chiaro, Anthony Megrant, Julian Kelly, Zijun Chen, Kevin Satzinger, Rami Barends, *et al.*, "Demonstrating a continuous set of two-qubit gates for near-term quantum algorithms," *Physical Review Letters* **125**, 120504 (2020).
- [37] Abhinav Kandala, Antonio Mezzacapo, Kristan Temme, Maika Takita, Markus Brink, Jerry M Chow, and Jay M Gambetta, "Hardware-efficient variational quantum eigensolver for small molecules and quantum magnets," *Nature* **549**, 242–246 (2017).
- [38] Jarrod R McClean, Sergio Boixo, Vadim N Smelyanskiy, Ryan Babbush, and Hartmut Neven, "Barren plateaus

- in quantum neural network training landscapes,” *Nature communications* **9**, 1–6 (2018).
- [39] Roeland Wiersema, Cunlu Zhou, Yvette de Sereville, Juan Felipe Carrasquilla, Yong Baek Kim, and Henry Yuen, “Exploring entanglement and optimization within the hamiltonian variational ansatz,” *PRX Quantum* **1**, 020319 (2020).
- [40] Austin G. Fowler, Matteo Mariantoni, John M. Martinis, and Andrew N. Cleland, “Surface codes: Towards practical large-scale quantum computation,” *Physical Review A* **86**, 032324 (2012).
- [41] Charles D Hill, Eldad Peretz, Samuel J Hile, Matthew G House, Martin Fuechsle, Sven Rogge, Michelle Y Simmons, and Lloyd CL Hollenberg, “A surface code quantum computer in silicon,” *Science advances* **1**, e1500707 (2015).
- [42] Christian Kraglund Andersen, Ants Remm, Stefania Lazar, Sebastian Krinner, Nathan Lacroix, Graham J Norris, Mihai Gabureac, Christopher Eichler, and Andreas Wallraff, “Repeated quantum error detection in a surface code,” *Nature Physics* **16**, 875–880 (2020).
- [43] R. Versluis, S. Poletto, N. Khammassi, B. Tarasinski, N. Haider, D. J. Michalak, A. Bruno, K. Bertels, and L. DiCarlo, “Scalable quantum circuit and control for a superconducting surface code,” *Physical Review Applied* **8** (2017), 10.1103/physrevapplied.8.034021.
- [44] For the sake of comparison of the gate count, we assume the same native gates as before. To the best of our knowledge, quantum computers that support both the essentially native implementation of the exchange interaction and kagome connectivity do not exist yet, so on current devices with all-to-all connectivity there will be some transpilation overhead.
- [45] Julia Kempe, Alexei Kitaev, and Oded Regev, “The complexity of the local hamiltonian problem,” *SIAM Journal on Computing* **35**, 1070–1097 (2006).
- [46] Stephen Piddock and Ashley Montanaro, “The complexity of antiferromagnetic interactions and 2d lattices,” *Quantum Information and Computation* **17**, 636–672 (2017).
- [47] Dorit Aharonov and Tomer Naveh, “Quantum NP - a survey,” (2002), [arXiv:quant-ph/0210077](https://arxiv.org/abs/quant-ph/0210077) [quantum-ph].
- [48] Attila Szabo and Neil S Ostlund, *Modern quantum chemistry: introduction to advanced electronic structure theory* (Courier Corporation, 2012).
- [49] Hsin-Yuan Huang, Richard Kueng, and John Preskill, “Efficient estimation of pauli observables by derandomization,” (2021), [arXiv:2103.07510](https://arxiv.org/abs/2103.07510).
- [50] The total spin operator is defined by  $\mathbf{S}^2 = \mathbf{S} \cdot \mathbf{S}$ , with  $\mathbf{S} = \sum_{i=1}^n \mathbf{S}^{(i)}$ , and is related to the total spin quantum number  $S$  by  $\mathbf{S}^2 |\psi\rangle = S(S+1) |\psi\rangle$  for eigenstates  $|\psi\rangle$  of  $\mathbf{S}^2$ . The total magnetization operator in the  $\alpha$ -direction is defined as  $\mathbf{S}_\alpha = \sum_{i=1}^n [\mathbf{S}^{(i)}]_\alpha$ , and is related to the magnetization quantum number  $S_z$  by  $\mathbf{S}_z |\psi\rangle = S_z |\psi\rangle$  for eigenstates  $|\psi\rangle$  of  $\mathbf{S}_z$ .  $\mathbf{S}^2$  and  $\mathbf{S}_z$  commute, and are hence simultaneously diagonalizable. Acting with the ladder operator  $\mathbf{S}_\pm = \mathbf{S}_x \pm i\mathbf{S}_y$  on a state with quantum number  $S_z$  raises (lowers) the  $S_z$  quantum number of that state with unity, for as long as the new value of  $S_z$  lays between  $-S$  and  $S$ , and annihilates that state otherwise. The Hamiltonian, circuit  $C$  and  $|\psi_{\text{init}}\rangle\langle\psi_{\text{init}}|$  all commute with  $\mathbf{S}_x$ ,  $\mathbf{S}_y$  and  $\mathbf{S}_z$  (and hence with  $\mathbf{S}^2$  and  $\mathbf{S}_\pm$ ), and therefore have a  $SU(2)$  symmetry. See e.g. Ref. [70] for more details.
- [51] For the HAFM on the chain, there is formal proof that the ground state indeed lays within the  $S = 0$  sector, for example via the Bethe ansatz [23] or through the more general result by Lieb and Mattis [71]. For the (tripartite) kagome lattice, such formal proof is unknown. There is, however, substantial evidence that  $S = S_z = 0$  for the ground state of the HAFM on (patches of) the kagome lattice [2, 5, 19, 52–54].
- [52] P. Lecheminant, B. Bernu, C. Lhuillier, L. Pierre, and P. Sindzingre, “Order versus disorder in the quantum heisenberg antiferromagnet on the kagomé lattice using exact spectra analysis,” *Physical Review B* **56**, 2521–2529 (1997).
- [53] P. Sindzingre and C. Lhuillier, “Low-energy excitations of the kagomé antiferromagnet and the spin-gap issue,” *EPL (Europhysics Letters)* **88**, 27009 (2009).
- [54] Hiroki Nakano and Toru Sakai, “Numerical-diagonalization study of spin gap issue of the kagome lattice heisenberg antiferromagnet,” *Journal of the Physical Society of Japan* **80**, 053704 (2011).
- [55] Kazuhiro Seki, Tomonori Shirakawa, and Seiji Yunoki, “Symmetry-adapted variational quantum eigensolver,” *Physical Review A* **101** (2020), 10.1103/physreva.101.052340.
- [56] X. Bonet-Monroig, R. Sagastizabal, M. Singh, and T. E. O’Brien, “Low-cost error mitigation by symmetry verification,” *Physical Review A* **98** (2018), 10.1103/physreva.98.062339.
- [57] Matthew J. S. Beach, Roger G. Melko, Tarun Grover, and Timothy H. Hsieh, “Making trotters sprint: A variational imaginary time ansatz for quantum many-body systems,” *Physical Review B* **100**, 094434 (2019).
- [58] Python Software Foundation, “Python language reference, version 2.8,” <https://docs.python.org/3.8/> (2019).
- [59] Charles R. Harris, K. Jarrod Millman, Stéfan J. van der Walt, Ralf Gommers, Pauli Virtanen, David Cournapeau, Eric Wieser, Julian Taylor, Sebastian Berg, Nathaniel J. Smith, Robert Kern, Matti Picus, Stephan Hoyer, Marten H. van Kerkwijk, Matthew Brett, Allan Haldane, Jaime Fernández del Río, Mark Wiebe, Pearu Peterson, Pierre Gérard-Marchant, Kevin Sheppard, Tyler Reddy, Warren Weckesser, Hameer Abbasi, Christoph Gohlke, and Travis E. Oliphant, “Array programming with NumPy,” *Nature* **585**, 357–362 (2020).
- [60] Royud Nishino and Shohei Hido Crissman Loomis, “Cupy: A numpy-compatible library for nvidia gpu calculations,” 31st conference on neural information processing systems, 151 (2017).
- [61] Michael A Nielsen, *Neural networks and deep learning*, Vol. 25 (Determination press, 2015).
- [62] Seiya Tokui, Kenta Oono, Shohei Hido, and Justin Clayton, “Chainer: a next-generation open source framework for deep learning,” in *Proceedings of workshop on machine learning systems (LearningSys) in the twenty-ninth annual conference on neural information processing systems (NIPS)*, Vol. 5 (2015) pp. 1–6.
- [63] Pauli Virtanen, Ralf Gommers, Travis E. Oliphant, Matt Haberland, Tyler Reddy, David Cournapeau, Evgeni Burovski, Pearu Peterson, Warren Weckesser, Jonathan Bright, Stéfan J. van der Walt, Matthew Brett, Joshua Wilson, K. Jarrod Millman, Nikolay Mayorov, Andrew R. J. Nelson, Eric Jones, Robert Kern, Eric Larson, C J

- Carey, İlhan Polat, Yu Feng, Eric W. Moore, Jake VanderPlas, Denis Laxalde, Josef Perktold, Robert Cimrman, Ian Henriksen, E. A. Quintero, Charles R. Harris, Anne M. Archibald, Antônio H. Ribeiro, Fabian Pedregosa, Paul van Mulbregt, and SciPy 1.0 Contributors, “SciPy 1.0: Fundamental Algorithms for Scientific Computing in Python,” *Nature Methods* **17**, 261–272 (2020).
- [64] Richard B Lehoucq, Danny C Sorensen, and Chao Yang, *ARPACK users’ guide: solution of large-scale eigenvalue problems with implicitly restarted Arnoldi methods* (SIAM, 1998).
- [65] J.I. Latorre, E. Rico, and G. Vidal, “Ground state entanglement in quantum spin chains,” *Quantum Information and Computation* **4**, 48–92 (2004).
- [66] Let us focus on  $KVQE_G$ , and lay out a coordinate system over the 24 qubits used in Fig. 2 (top right). We put the origin (0,0) at the bottom left qubit, the qubit directly above at (0,1), and the qubit directly to the right of the origin at (1,0). At  $p = 2$ , there is no qubit whose past light cone in  $C$  covers the entire system. At  $p = 3$ , there are qubits, such as the bottom right (4,0), bottom left (0,0), top left (0,4) and middle (2,2) qubits, whose past light cone in  $C$  covers the entire system. There are, however, still some qubits for which this is not the case, such as the qubits at (3,4), (4,3) and the top middle (2,0). At  $p = 4$ , the past light cone of the latter qubits covers the entire system, except for the qubit at (3,4). It is only after  $p = 5$  cycles that its past light cone covers the entire system.
- [67] Ruoyu Li, Luca Petit, David P Franke, Juan Pablo Dehollain, Jonas Helsen, Mark Steudtner, Nicole K Thomas, Zachary R Yocovits, Kanwal J Singh, Stephanie Wehner, *et al.*, “A crossbar network for silicon quantum dot qubits,” *Science advances* **4**, eaar3960 (2018).
- [68] Matthew P Harrigan, Kevin J Sung, Matthew Neeley, Kevin J Satzinger, Frank Arute, Kunal Arya, Juan Atalaya, Joseph C Bardin, Rami Barends, Sergio Boixo, *et al.*, “Quantum approximate optimization of non-planar graph problems on a planar superconducting processor,” *Nature Physics* **17**, 332–336 (2021).
- [69] Jan Lukas Bosse and Ashley Montanaro, “Probing ground state properties of the kagome antiferromagnetic heisenberg model using the variational quantum eigensolver,” (2021), [arXiv:2108.08086 \[quant-ph\]](https://arxiv.org/abs/2108.08086).
- [70] J. J. Sakurai and Jim Napolitano, *Modern Quantum Mechanics* (Cambridge University Press, 2020).
- [71] Elliott Lieb and Daniel Mattis, “Ordering energy levels of interacting spin systems,” *Journal of Mathematical Physics* **3**, 749–751 (1962).